The Effect of Deposition Conditions on Heterointerface-Driven Band Alignment and Resistive Switching Properties

Yong, Zhihua; Mamidala, Saketh, Ram; Persson, Karl-Magnus; Subramanian, Gomathy Sandhya ; Wernersson, Lars-Erik; Pan, Jisheng

Published in:
Advanced Electronic Materials

DOI:
10.1002/aelm.202200220

2022

Document Version:
Peer reviewed version (aka post-print)

The Effect of Deposition Conditions on Heterointerface-Driven Band Alignment and Resistive Switching Properties

Zhihua Yong,[†,*] Mamidala Saketh Ram,[‡] Karl-Magnus Persson,[‡] Gomathy Sandhya Subramanian,[§,‖] Lars-Erik Wernersson,[‡,*] Jisheng Pan.[§,*]

[†]Singapore University of Technology and Design (SUTD), 8 Somapah Road, 487372, Singapore

[‡]Department of Electrical and Information Technology, Lund University, Box 118, Lund 221 00, Sweden

[§]Institute of Materials Research and Engineering, Agency for Science, Technology and Research (A*STAR), 2 Fusionopolis Way, Innovis, #08-03, Singapore 138634

[‖] Singapore Institute of Food and Biotechnology Innovation, Agency for Science, Technology and Research (A*STAR), 31 Biopolis Way, #01-02 Nanos, Singapore 138669

*Address correspondence to: Zhihua Yong, a0002321@u.nus.edu, Jisheng Pan, js-pan@imre.a-star.edu.sg, Lars-Erik Wernersson, lars-erik.wernersson@eit.lth.se

Keywords

band alignment, X-ray photoelectron spectroscopy, atomic layer deposition, resistive switching, RRAM, hafnium oxide, titanium nitride

ABSTRACT

Titanium nitride and hafnium oxide stack have been widely used in various resistive memory elements since the materials are complementary-metal-oxide-semiconductor compatible. The understanding of the interface properties between the electrode and the oxide is important in designing the memory behavior. To bridge this understanding, we compare HfO_x grown using plasma enhanced atomic layer deposition (PEALD) and thermal atomic layer deposition (TALD), in terms of band alignment and electrical performances in the HfO_x/PEALD TiN stacks. X-ray photoelectron spectroscopy reveals a thicker interfacial TiO_2 layer in the PEALD HfO_x/TiN stack whose interface resembles more to the PEALD HfO_x/TiO_2 interface (Conduction band offset ΔE_C = 1.63 eV), whereas the TALD HfO_x stack interface resembles more to the TALD HfO_x/TiN interface (ΔE_C = 2.22 eV). The increase in the forming voltage and the early onset of reverse filament formation (RFF) in the I-V measurements for the PEALD HfO_x stack confirms the presence of the thicker interfacial layer; the early onset of RFF is likely related to a smaller ΔE_C. Our findings show the importance of understanding the intricate details of the material stack, where ΔE_C difference and the presence of a thicker TiO_2 interfacial layer due to different deposition procedures affect the device performance.

1. Introduction

Oxygen vacancy resistive-random-access-memories (RRAM), due to being non-volatile, highly scalable and fast, are ideal candidates suitable to meet the future computational/memory needs beyond the classical von-Neumann computing architecture.[1-3] More specifically, indium-tin-oxide (ITO)/HfO_2 based RRAM have shown promise to be used in dense cross-point arrays due to their ultra-low switching voltages and self-compliance properties.[2, 4] Emerging non-volatile memory technologies that consist of a metal-insulator-metal (MIM) stack, such as oxygen vacancy filamentary switching memories (OxRRAM), as well as ferroelectric switching memories (FeRAM) that often use the same material combination, represent a low complexity solution for large scale integration of fast and energy efficient non-volatile memories.[5-7] In particular, ITO/HfO_2/TiN based OxRRAMs have shown promise to be used in dense and highly energy efficient cross-point arrays due to their ultra-low switching voltages.[4, 8] In order to increase the maturity of the different RRAM technologies, we need to gain a more in-depth understanding of how the deposition conditions affect the material properties at the interfaces, the composition of the oxide, and the performance of the RRAM devices.

To enable dense integration, it is vital to scale down the switching oxide thickness while retaining the RRAM performance and as a result, the interface properties will become increasingly important. [9] In this study, we utilize relevant ultra-scaled oxide thicknesses (~3 nm) and compare the HfO_x deposited by TALD and PEALD techniques. The deposition techniques differ by the reactions used to remove ligands from the adsorbed metal precursor. In TALD, heat provides sufficient energy to facilitate the desired chemical reactions on the surface whereas in PEALD, highly reactive species that were generated from the reactant by a plasma discharge induces reactions at lower temperature. So far, there have been few comparative studies[10-12] between the electrical properties of the TALD and PEALD hafnium oxide. Furthermore, no study has been performed to correlate the electronic band profiles of the TALD and PEALD HfO_x/TiN interfaces in the OxRRAM devices with the electrical performance of the TALD and the PEALD HfO_x OxRRAM devices. In this respect, X-ray photoelectron spectroscopy (XPS) is a powerful and non-destructive technique used to study the elemental components of the semiconductor heterostructures and is an appropriate technique to determine the band alignment at the heterointerfaces.

In this work, two types of OxRRAM stacks were fabricated, consisting of a TiN bottom metal electrode (BME), a HfO_x switching oxide layer, and an ITO top metal electrode (TME), and where the two types only differ by the fabrication procedures of the HfO_x switching oxide layer, using either TALD or PEALD. A thicker interfacial TiO_2 layer was observed via X-ray photoelectron spectroscopy (XPS) in the PEALD HfO_x/TiN stack, together with the presence of sub-oxides in the PEALD HfO_x layer. The valence band offset (ΔE_V) values for TALD and PEALD HfO_x/TiN heterojunctions are calculated to be 2.91 eV and 3.28 eV, respectively. The band gap values for the TALD and PEALD HfO_x samples are 5.13 eV and 5.02 eV, respectively. The ΔE_C values for the TALD and the PEALD HfO_x/TiN heterojunctions are 2.22 eV and 1.74 eV, respectively. The ΔE_C value is about 0.5 eV higher for TALD HfO_x/TiN sample while the ΔE_V value is 0.37 eV higher for PEALD HfO_x/TiN sample. However, when we take the TiO_2 interfacial layer between the HfO_x layer and ALD TiN BME into consideration, the calculated ΔE_C values for the TALD HfO_x/TiO_2 and the PEALD HfO_x/TiO_2 heterojunctions shrink to 1.70 eV and 1.63 eV, respectively whereas the calculated ΔE_V values for the TALD HfO_x/TiO_2 and the PEALD HfO_x/TiO_2 heterojunctions shrink to 0.44 eV and 0.40 eV, respectively. In this case, the difference of their ΔE_C and and ΔE_V values decrease, the ΔE_C and ΔE_V are higher for TALD HfO_x/TiO_2. All the band alignment of the TALD HfO_x/TiN, PEALD HfO_x/TiN, TALD HfO_x/TiO_2 and PEALD HfO_x/TiO_2 heterostructures is classified under type I: straddling gap. Both the Hf 4*f* XPS spectra and valence band (VB) studies indicate that the PEALD HfO_x is more oxygen deficient than the TALD HfO_x. The presence of the interfacial TiO_2 layer is confirmed electrically by an increased forming voltage (V_{FORM}) due to a larger effective oxide thickness in the PEALD HfO_x sample. When the OxRRAM is operated at relevant current levels (sub 100 µA), it becomes more sensitive to the formation of parasitic vacancies due to fewer vacancies being involved in the switching. The oxygen vacancy filament is found to be less stable when the switching oxide HfO_x is deposited using PEALD instead of TALD. When PEALD HfO_x is used, a vacancy reservoir in the form of an interfacial TiO_2 layer reduces ΔE_C between the PEALD HfO_x and TiN, which makes it more prone to the formation of parasitic oxygen vacancies which is confirmed by the VB studies. Parasitic oxygen vacancies can lead to RFF where vacancies stemming from the TiO_2/BME reforms the ruptured filament. By understanding how the different fabrication methods affect the composition and the band alignment of the oxide interface/BME, it is possible to optimize the stack integration for improved performance, which is critical in elevating the technology maturity for both high performance OxRRAMs and FeRAMs implementations.

2. Results and discussion

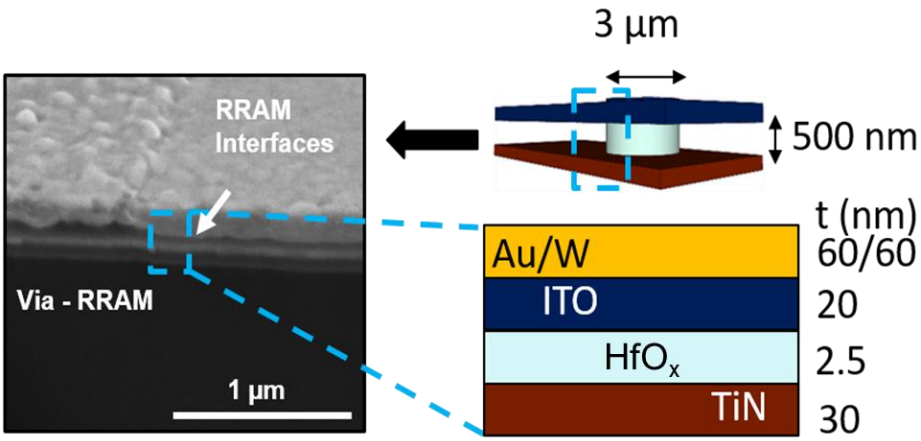

Figure 1. A cross-sectional SEM image and schematics depicting the studied RRAM via structure, as well as the deposited layers in the RRAM-stack. To contact the etched out TiN bottom electrode, vias were etched into an organic spacer (lifting layer). Thickness (t) of the fabricated RRAM material layers is indicated.

The cross-sectional Scanning Electron Microscope (SEM) image and an overview of the model of the RRAM samples are shown in Figure 1. Details of the fabrication work are discussed in Section 4.1.

2.1 Interface studies of thin HfO_x by XPS

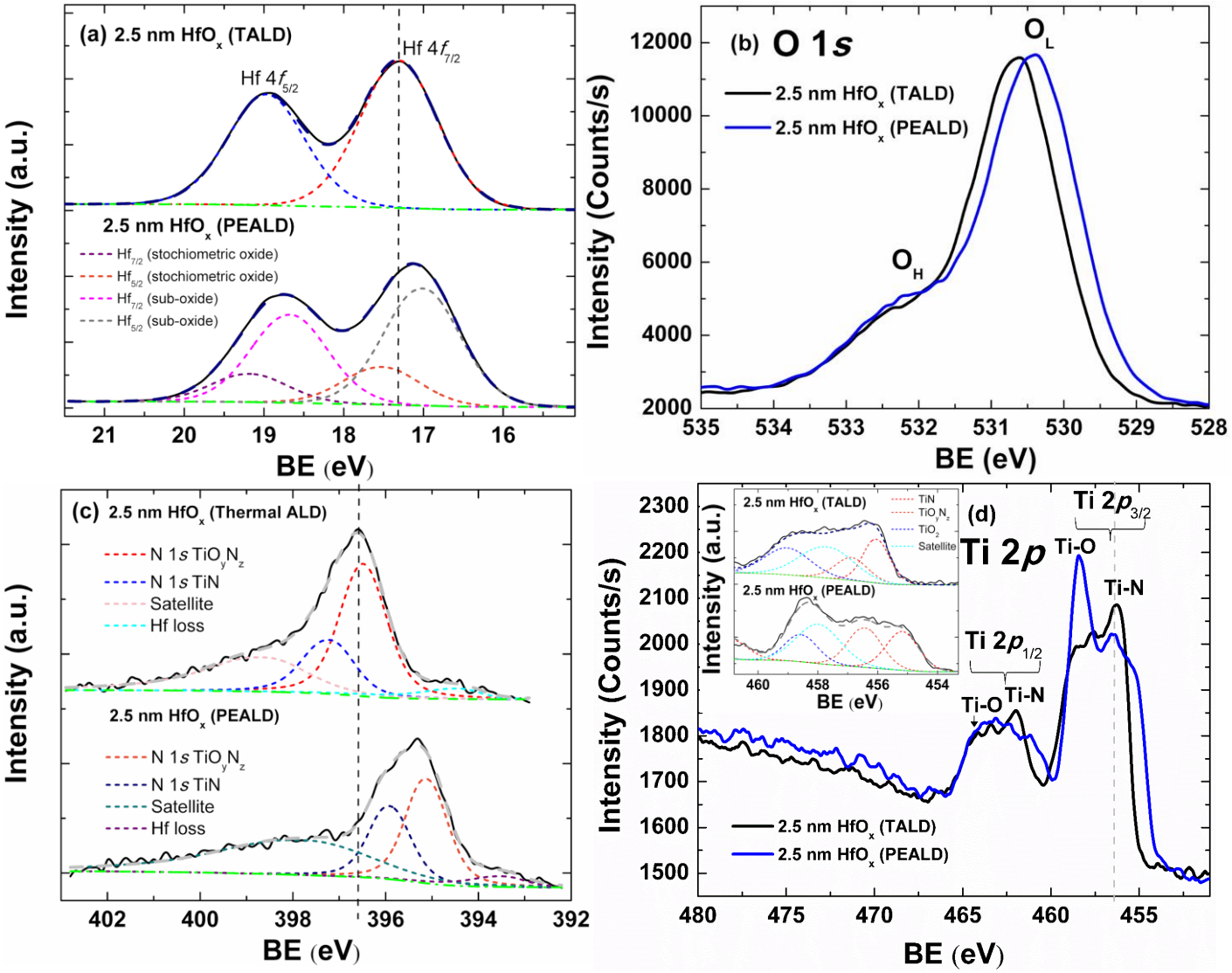

Figure 2. (a) Fitted Hf 4*f* XPS spectra, (b) fitted O 1*s* XPS spectra, (c) fitted N 1*s* XPS spectra and (d) Ti 2*p* XPS spectra of the 2.5 nm TALD HfO_x and PEALD HfO_x. Inset of (d) shows the fitted Ti $2p_{3/2}$ spectra of the 2.5 nm TALD HfO_x and PEALD HfO_x. C 1s peak from adventitious carbon at 285.35 eV was used as a reference for charge correction.

Table 1: XPS analysis data for 2.5 nm HfO_x samples. Error bar of XPS core level spectra lies within ±0.05 eV.

Sample ID	BE (Hf $4f_{7/2}$) [eV]	FWHM (Hf $4f_{7/2}$) [eV]	Hf $4f_{7/2}$ Sub: Main Ratio	BE (N 1*s* - TiN) [eV]	BE (Ti $2p_{3/2}$ – TiO_2) [eV]
2.5 nm TALD HfO_x	17.31	1.13	-	397.61	458.92
2.5 nm PEALD HfO_x	17.51 (17.00)[a]	1.13 (1.13)[a]	3.12	396.71	458.54

[a]Refers to the oxygen deficient Hf sub-species.

Three sets of samples were prepared for XPS measurements for the surface, interface and the band alignment studies: (1) PEALD and TALD HfO_x (2.5 nm)/TiN (30 nm) heterostructures deposited on Si substrate to determine the binding energy (BE) difference between the Hf $4f_{7/2}$ and N 1*s*/ Ti $2p_{3/2}$ core levels at the interface of HfO_x/TiN heterojunction, (2) a 15 nm thick HfO_x layer deposited on 30 nm TiN which was first grown on Si substrate to measure the BE difference between the valence band maximum (VBM) and the Hf $4f_{7/2}$ core level of bulk HfO_x, and (3) a 30 nm thick TiN film grown on Si substrate to measure the BE difference between the VBM and N 1*s* core-level of bulk TiN. Additionally, a 0.1 cm thick TiO_2 annealed single crystalline rutile substrate was also included in the XPS measurements to determine the BE difference between the VBM and the Ti $2p_{3/2}$ core level of bulk TiO_2. The XPS results for these samples were shown in Figures 1 – 3 and Tables 1 - 3.

Figure 2a shows the fitted Hf 4*f* spectra of the 2.5 nm HfO_x films after an iterated Shirley-type background subtraction. The adventitious carbon located at 285.35 eV was used as a reference for charge correction. The Hf 4*f* spin–orbit (SO) splitting was fixed at 1.66 eV and the branching ratio of Hf $4f_{7/2}$ peak to Hf $4f_{5/2}$ peak was kept to 1.33.[5] The fitted results were tabulated in Table 1. Only one doublet is needed to achieve a good fit for the Hf 4*f* spectra of the TALD HfO_x whereas two doublets are required to obtain a good fit for the Hf 4*f* spectra of the PEALD HfO_x. The additional doublet component at lower BE in the PEALD HfO_x spectra is ascribed to non-stoichiometric hafnium oxide. This implies that PEALD HfO_x has more oxygen deficient hafnium sub-species than the TALD HfO_x.

The fitted O 1*s* and N 1*s* spectra after an iterated Shirley-type background subtraction are displayed in Figures 2b and 2c, respectively. Both the O 1*s* spectra consist of two peaks: a clear peak at lower BE and a small shoulder at higher BE. The peak at lower BE (O_L) can be assigned to the O^{2-} ion under fully oxidized stoichiometric conditions – oxygen in HfO_2 lattice, whereas the shoulder peak at higher BE (O_H) is ascribed to the bridging hydroxyls. The fitted N 1*s* spectra in Figure 2c consist of the following: plasmon loss feature of the Hf $4p_{3/2}$, N 1*s* features of TiO_yN_z and TiN, plasmon loss feature of the Hf $4p_{3/2}$ and a satellite feature of the TiN, in the order of increasing BE. The peak area ratio of TiO_yN_z to TiN is higher for the PEALD HfO_x. This suggests that PEALD HfO_x contains more titanium oxynitride than TALD HfO_x. Furthermore, BE of the N 1*s* peak that corresponds to the Ti-N species found in the BME of the TALD HfO_x sample is shifted by 0.9 eV (Table 1) with respect to that of the PEALD HfO_x sample.

The Ti 2*p* XPS results were plotted in Figure 2d. The main components of the Ti 2*p* spectra consist of the following: Ti 2*p* ($2p_{3/2}$ and $2p_{1/2}$) doublet peaks of TiO_2,[13] shake-up satellite peaks of TiN, Ti 2*p* doublet peaks of TiO_yN_z and TiN,[14, 15] in the order of decreasing BE. The Ti 2*p* SO splitting values for TiO_2, TiO_xN_y and TiN were fixed at 5.80 eV, 5.70 eV and 5.70 eV, respectively, while the branching ratio of Ti $2p_{3/2}$ peak to Ti $2p_{1/2}$ peak was kept to 2. The Ti 2*p* XPS peak fitting results are shown in the inset of Figure 2d. The BE of the Ti $2p_{3/2}$ peak that corresponds to the Ti-O species found in the BME of the TALD HfO_x sample is shifted by 0.38 eV (Table 1) with respect to that of the PEALD HfO_x sample. The origin of the shake-up satellite feature might be attributed to the decrease in the screening probability of the core-hole created during photoionization by Ti 3*d* electrons[16, 17] or even caused by structural effects.[18] As the density of states of TiN near and at the Fermi level is high, there will be simultaneous excitations of valence electrons which lead to energy loss. Thus, asymmetric functions will be required for the fitting of the Ti 2*p* doublet of the TiN species.

By comparing the Ti $2p_{3/2}$ peak height ratio of Ti-O to Ti-N, we find that the PEALD HfO_x has a much thicker TiO_2 interfacial layer as compared to the TALD HfO_x. During the first few cycles of PEALD, the precursor molecules were chemisorbed to the surface but steric hindrance from these precursor molecules will restrict HfO_x deposition to a partial monolayer over an individual deposition cycle.[11, 19, 20] The subsequent plasma oxygen will replace the organic ligands with oxygen and might oxidize the TiN BME to form native oxide (TiO_2) when the rate of TiN oxidation exceeds the rate of self-cleaning effect of TiO_2 during dosing of the TEMA-Hf precursor in HfO_2 ALD.[21] On the other

hand, during TALD, water will oxidize the highly reactive chemisorbed organometallic precursor but will not react directly with the TiN BME during the formation of HfO_x.

2.2 Valence Band studies of thin HfO_x by XPS

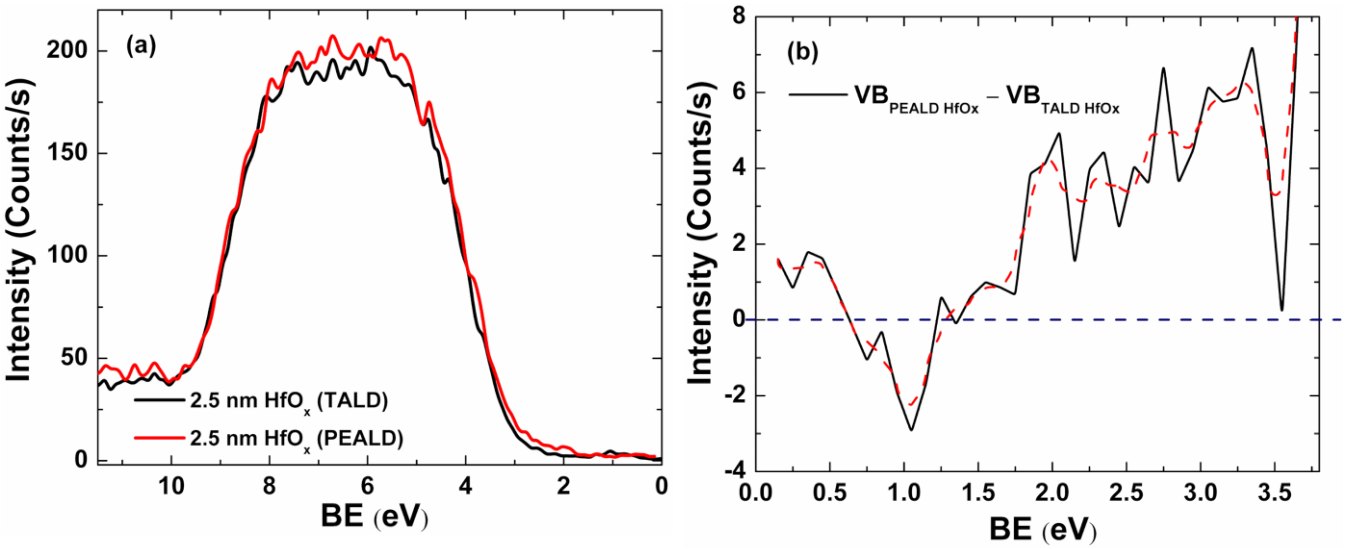

Figure 3. (a) VB XPS spectra of the 2.5 nm TALD HfO_x and PEALD HfO_x samples and (b) their corresponding difference spectra (black line) and smoothed data (dashed red line) in the 0 – 3.6 eV BE range are shown. Dashed lines serve as visual guide.

To compare the amount of oxygen vacancies in HfO_x, the VB XPS spectra of the 2.5 nm TALD and PEALD HfO_x samples were plotted in Figure 3a and the difference between the two VB spectra were depicted in Figure 3b. On top of that, theoretical calculations[22] were researched upon to gain further insight in the comparison. Perevalov et al.[22] have performed DFT simulations using the plane-wave as a basis set and pseudopotential approximation to generate the electronic structure of HfO_2. They reported that a single neutral oxygen vacancy creates one gap state which is doubly occupied and lies at 3.3 eV and 3.0 eV above the VB edge for monoclinic and orthorhombic HfO_2, respectively, and this defect level is primarily formed by 5*d* and 6*s* states of Hf atoms. Their results were also verified experimentally[23] in the VB spectra of non-stoichiometric HfO_x films which showed the formation of electronic states at 3 eV above the top of VB. The PEALD and TALD HfO_x samples are amorphous since no crystal phase related to HfO_2 was observed in the XRD diffraction patterns. Despite the amorphous nature of the PEALD and TALD HfO_x samples, the atomic short-range order will remain to some extent even when the atomic order in the long range ceases to exist, thus the band-like structures of the electron energy states are similar to those of the crystalline HfO_x.

The difference spectra in Figure 3b, therefore, implies that the PEALD HfO_x has more oxygen vacancies than the TALD HfO_x and this agrees with our XPS results which indicates that the PEALD HfO_x has oxygen deficient hafnium sub-species which is absent in the TALD HfO_x. This intensity difference in the region around 3 eV between the VB spectra of the TALD HfO_x and PEALD HfO_x is much smaller as compared to the corresponding thicker 15 nm samples, as seen in Figure 4c. This fact supports the notion that the difference is related to the bulk properties of the HfO_x film and not related to an interface effect.

2.3 Surface and interface studies of thick HfO_x by XPS

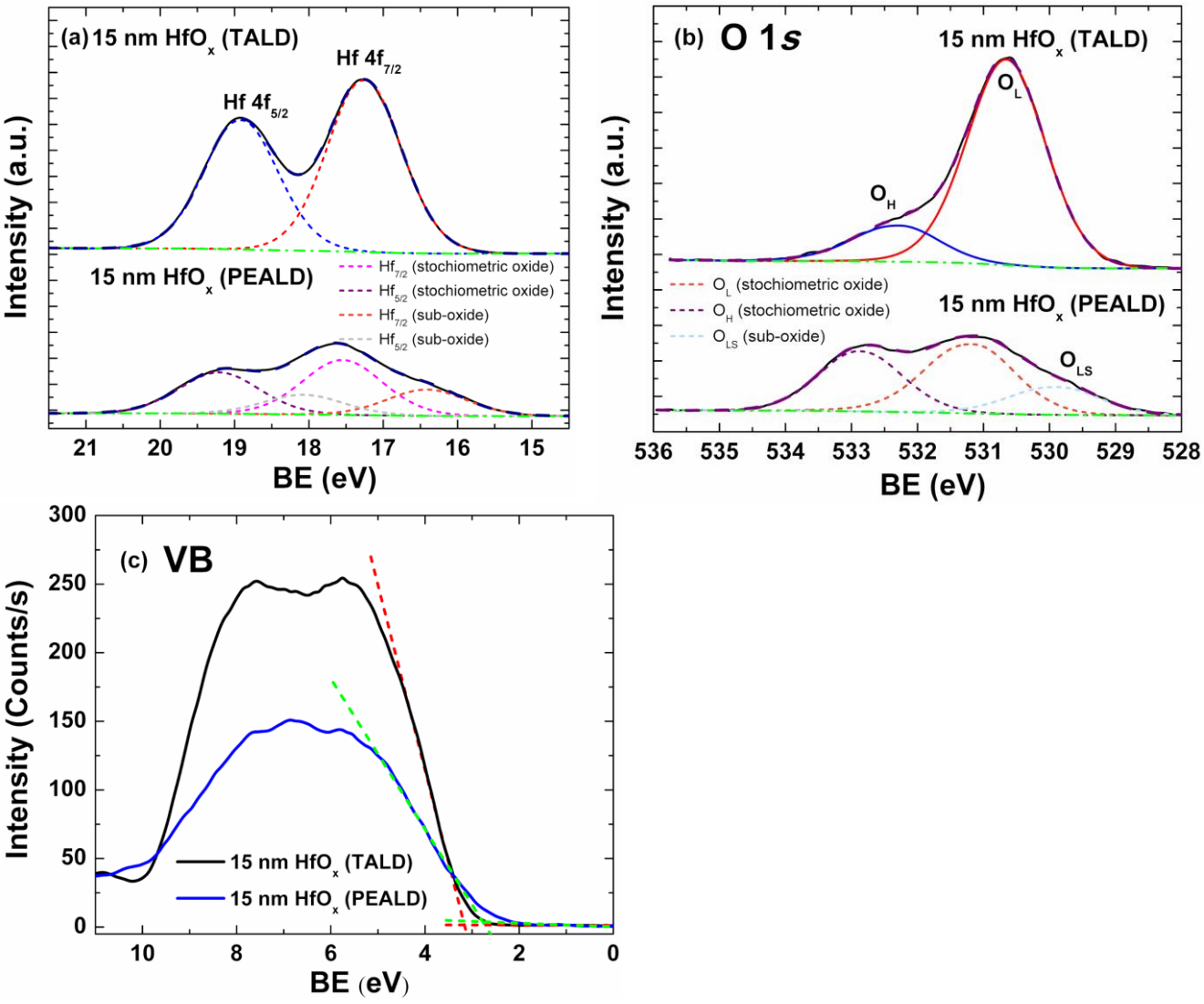

Figure 4. (a) Fitted Hf 4*f* XPS spectra, (b) O 1*s* XPS spectra and (c) Valence band spectra of the 15 nm TALD HfO_x and PEALD HfO_x. C 1s peak from adventitious carbon at 285.35 eV was used as a reference for charge correction.

Table 2: XPS analysis data for 15 nm HfO_x samples. Error bar of XPS core level spectra lies within ±0.05 eV.

Sample ID	BE (Hf $4f_{7/2}$) [eV]	FWHM (Hf $4f_{7/2}$) [eV]	O_H/O_L Ratio	VBM [eV]
15 nm TALD HfO_x	17.24	1.17	0.20	3.16
15 nm PEALD HfO_x	17.55	1.26	0.57	2.74
	(16.41)[a]	(1.26)[a]		

[a]Refers to the oxygen deficient Hf sub-species.

The XPS results for 15 nm PEALD and TALD HfO_x were displayed in Figure 4a. C 1s peak from adventitious carbon at 285.35 eV was used as a reference for charge correction. It was observed that after an iterated Shirley-type background subtraction, the Hf 4*f* spectrum can be fitted by one doublet for the 15 nm TALD HfO_x sample. The Hf 4*f* SO splitting was fixed at 1.66 eV and the branching ratio of Hf $4f_{7/2}$ peak to Hf $4f_{5/2}$ peak was kept to 1.33.[5] On the other hand, two doublets are required to produce a good fit for the Hf 4*f* spectrum of the 15nm PEALD HfO_x sample. These results and the BE of the Hf 4*f* core levels are quite consistent with those of the respective 2.5 nm HfO_x films (Figure 2a). This further corroborates that HfO_x grown using PELAD produces more oxygen deficient hafnium sub-species than HfO_x fabricated using TALD.

Figure 4b shows the fitted O 1*s* spectra of ~15 nm PEALD and TALD HfO_x, after an iterated Shirley-type background subtraction. The O 1*s* spectra of 15 nm TALD HfO_x sample can be de-convoluted into two peaks- O_L peak at lower BE and O_H peak at higher BE. However, three peaks are required to fit the O 1*s* spectra of 15 nm PEALD HfO_x sample, with an addition of a third peak (O_{LS}) at an even lower BE. This peak is attributed to the oxide with a higher valence state (> -2) under partially oxidized conditions. This further affirms that PELAD HfO_x is more oxygen deficient than TALD HfO_x. The fitted results were summarized in Table 2. The 15 nm PEALD HfO_x is likely to be much more defective than the 15 nm TALD HfO_x since the PEALD HfO_x has a lot more hydroxyl groups (O_H/O_L Ratio) attached to the surface, as compared to TALD HfO_x.

The VB XPS spectra for the 15 nm PEALD and TALD HfO_x are shown in Figure 4c. The valence band maximum (VBM) positions were determined by the intersection of the linear extrapolation of the leading edge of the VB spectrum and the background. This method is widely utilized to achieve high accuracy in the VBM position of semiconductors. The VBM values of the 15 nm TALD and PEALD HfO_x samples were found to be 3.16 and 2.74 eV (Table 2), respectively, corroborating that the PEALD HfO_x is more oxygen deficient than TALD HfO_x. Due to the formation of gap states around 3 eV above the top of VB in non-stoichiometric HfO_x films, the more oxygen deficient PEALD HfO_x will have a smaller VBM value than the TALD HfO_x, which is consistent with the fitting results of the Hf 4*f* core-level peaks.

2.4 Band alignment studies

2.4.1 Theories

According to the Kraut's method,[24] ΔE_V of the HfO_x/TiN heterojunction can be calculated using the formula:

$$\Delta E_V = \underbrace{(E_{Hf\ 4f_{7/2}}^{HfO_x/TiN} - E_{N\ 1s}^{HfO_x/TiN})}_{\text{Thin sample}} + (E_{N\ 1s}^{TiN} - E_{VBM}^{TiN}) - \underbrace{(E_{Hf\ 4f_{7/2}}^{HfO_x} - E_{VBM}^{HfO_x})}_{\text{thick sample}} \quad \text{--- (1)}$$

Where E_l^S denotes the BE of the core level l in sample S; $(E_{Hf\ 4f_{7/2}}^{HfO_x/TiN} - E_{N\ 1s}^{HfO_x/TiN})$ is the BE difference measured by XPS in the 2.5 nm HfO_x/TiN thin heterojunction sample; $(E_{N\ 1s}^{TiN} - E_{VBM}^{TiN})$ and $(E_{Hf\ 4f_{7/2}}^{HfO_x} - E_{VBM}^{HfO_x})$ are the energy differences measured by XPS in the 30 nm TiN and the 15 nm HfO_x thick samples, respectively, where the Hf $4f_{7/2}$ BE of the fully oxidized Hf^{4+} is taken into account. The Ti 2*p* BE and VB studies of TiN are discussed in the Supporting Information Figures S1a and S1b, respectively. From the measurements, the calculated ΔE_V values (Table 3) for TALD and PEALD HfO_x/TiN heterojunctions are 2.91 eV and 3.28 eV, respectively.

In a similar way, ΔE_V of the HfO_x/TiO_2 heterojunction can be calculated using the formula:

$$\Delta E_V = \underbrace{(E_{Hf\ 4f_{7/2}}^{HfO_x/TiO_2} - E_{Ti\ 2p}^{HfO_x/TiO_2})}_{\text{Thin sample}} + (E_{Ti\ 2p}^{TiO_2} - E_{VBM}^{TiO_2}) - \underbrace{(E_{Hf\ 4f_{7/2}}^{HfO_x} - E_{VBM}^{HfO_x})}_{\text{thick sample}} \quad \text{--- (2)}$$

Where E_l^S denotes the BE of the core level l in sample S; ($E_{Hf\ 4f_{7/2}}^{HfO_x/TiO_2} - E_{Ti\ 2p}^{HfO_x/TiO_2}$) is the BE difference measured by XPS in the 2.5 nm HfO_x/TiO_2 thin heterojunction sample; ($E_{Ti\ 2p}^{TiO_2} - E_{VBM}^{TiO_2}$) and ($E_{Hf\ 4f_{7/2}}^{HfO_x} - E_{VBM}^{HfO_x}$) are the energy differences measured by XPS in the 0.1 cm thick annealed TiO_2 substrate and the 15 nm HfO_x thick samples, respectively, where the Hf $4f_{7/2}$ BE of the fully oxidized Hf^{4+} is taken into account. The Ti $2p$ BE and VB studies of TiO_2 are discussed in the Supporting Information Figures S1c and S1d, respectively. The calculated ΔE_V values from the measurements (Table 3) for TALD and PEALD HfO_x/TiO_2 heterojunctions are 0.44 eV and 0.40 eV, respectively.

2.4.2 Band gap measurements of HfO_x, TiN and TiO_2 by UV-Visible spectroscopy

To infer ΔE_C based on the value of ΔE_V, we first need to measure the band gap (E_g) of the HfO_x layer. In 1966, Tauc proposed a method of estimating the E_g value of amorphous semiconductors using optical absorption spectra,[25] which was further developed by Davis and Mott.[26] The energy-dependent absorption coefficient α can be determined by the following relationship using the Tauc method:

$$(\alpha h\nu)^{1/n} = A(h\nu - E_g) \quad \text{--- (3)}$$

where h is the Planck constant, ν is the photon's frequency of vibration, and A is a proportional constant. The value of n depends on the nature of the electron transition as follow:

For direct allowed transition: $n = \frac{1}{2}$

For direct forbidden transition: $n = \frac{3}{2}$

For indirect allowed transition: $n = 2$

For indirect forbidden transition: $n = 3$

Based on the theory that was reported by P. Kubelka and F. Munk[27] in 1931, the measured reflectance spectra can be transformed to the corresponding absorption spectra by applying the Kubelka−Munk function $F(R_\infty)$ as follow:

$$F(R_\infty) = \frac{k}{s} = \frac{(1 - R_\infty)^2}{2R_\infty} \quad \text{--- (4)}$$

where the diffuse reflectance $R_\infty = \frac{R_{sample}}{R_{standard}}$ is the reflectance of an infinitely thick sample, while *k* and *s* are the absorption and scattering coefficients of the sample, respectively. $F(R_\infty)$ is proportional to the absorption coefficient α. By replacing α with $F(R_\infty)$ in equation (3), a modified Kubelka–Munk function can be obtained as follow:

$$[F(R_\infty) \cdot h\nu]^{1/n} = A(h\nu - E_g) \quad \text{--- (5)}$$

Substituting (3) into (4), we get:

$$[\frac{(1 - R_\infty)^2}{2R_\infty} \cdot h\nu]^{1/n} = A(h\nu - E_g) \quad \text{--- (6)}$$

Since HfO_2 has an indirect allowed band gap, n is selected to be 2.[28, 29]

The acquired diffuse reflectance data from the 15 nm TALD and PEALD HfO_x samples were converted to the modified Kubelka-Munk function using equation (6) and plotted against the photon energy in Figures 5a and 5b, respectively. Due to the additional reflectance contribution from the 30 nm TiN layer and Si substrate beneath the HfO_x layer, the baseline approach method[30] was utilized to extract the band gap of the HfO_x, where the intersection between the linear fits of the fundamental peak and the slope below the fundamental absorption gives the E_g estimation, as shown in Figures 5a - 5b. The extracted E_g values (Table 3) for the 15 nm TALD and PEALD HfO_x samples are 5.13 eV and 5.02 eV, respectively. These values are consistent with the E_g value reported earlier in amorphous HfO_x [10] and HfO_2 nanoparticles[29, 31] and are lower than the band gap of crystallized monoclinic HfO_2 which ranges from 5.25 – 5.65 eV.[32] In addition, the measured band gap values are also slightly lower than some other reported values of amorphous HfO_2 in the literature,[32, 33] possibly as a result of the presence of defects like oxygen vacancies and oxygen interstitials, distortions on the HfO_6 octahedra due to defects and strain and intrinsic surface effects. [29] These factors might have induced the formation of intermediate levels between the VB and conduction band (CB), leading to the reduction in E_g.

On the other hand, TiN is metallic, hence it has no band gap. TiN has high melting point, low electrical resistivity and high thermal conductivity[34] and thin TiN films have been utilized as metal gate and diffusion barrier in modern integrated circuits. The UV–Visible absorption spectrum of the annealed rutile TiO_2 substrate is displayed in Figure 5c. The E_g of TiO_2 was determined to be about

2.99 eV via the Tauc plot method by calculating the intersection of the extrapolation of the linear portion of the curve with the background. n = $^3/_2$ was selected in the Tauc plot since rutile TiO_2 has a direct forbidden band gap.[35, 36]

2.4.3 Results

Together with the calculated ΔE_V and determined E_g values, we are able to calculate ΔE_C. All the values are tabulated in Table 3. The computed ΔE_C values for the TALD HfO_x/TiN and the PEALD HfO_x/TiN heterojunctions are 2.22 eV and 1.74 eV, respectively. There is a significant increment of about 0.5 eV for the ΔE_C value of the TALD HfO_x/TiN, as compared to the PEALD HfO_x/TiN that needs an explanation. The computed ΔE_V values for the TALD HfO_x/TiN and the PEALD HfO_x/TiN heterojunctions are 2.91 eV and 3.28 eV, respectively. There is a significant decrease of about 0.4 eV for the ΔE_V value of the TALD HfO_x/TiN, as compared to the PEALD HfO_x/TiN. When we take the TiO_2 interfacial layer between the HfO_x layer and ALD TiN BME into consideration, the calculated ΔE_C values for the TALD HfO_x/TiO_2 and the PEALD HfO_x/TiO_2 heterojunctions decrease to 1.70 eV and 1.63 eV, respectively, while the calculated ΔE_V values for the TALD HfO_x/TiO_2 and the PEALD HfO_x/TiO_2 heterojunctions decrease to 0.44 eV and 0.40 eV, respectively. This leads to a reduction in both the difference of the ΔE_C and ΔE_V values between the TALD HfO_x/TiO_2 and the PEALD HfO_x/TiO_2 but ΔE_C and ΔE_V of the TALD HfO_x/TiO_2 are higher. In the 2.5 nm PEALD HfO_x sample, the interfacial TiO_2 layer is clearly much thicker than the TiO_2 layer in the 2.5 nm TALD HfO_x sample, as observed from Figure 2d where the Ti-O signal is much stronger. Due to the presence of this thicker interfacial TiO_2 layer in the PEALD HfO_x/TiN stack, the interface of the 2.5 nm PEALD HfO_x sample will resemble more of the PEALD HfO_x/TiO_2 interface (ΔE_C = 1.63 eV and ΔE_V = 0.40 eV) whereas the interface of the 2.5 nm TALD HfO_x sample might be closer to TALD HfO_x/TiN interface (ΔE_C = 2.22 eV and ΔE_V = 2.91 eV), leading to a significant ΔE_C difference of 0.6 eV. The ~0.6 eV difference between the TALD and PEALD HfO_x samples has a significant impact on the RRAM operation of the two corresponding device stacks and this will be further discussed in the electrical data section 2.5.

Based on the evaluation for the band gaps and the band alignments, we now determine the corresponding band structures. The schematic diagrams of the band offset at the HfO_x/TiN heterojunction interface for TALD HfO_x and PEALD HfO_x are depicted in Figures 5d and 5e, respectively, while those at the HfO_x/TiO_2 heterojunction interface for TALD HfO_x and PEALD HfO_x

are displayed in Figures 5f and 5g, respectively. All the band alignment of the TALD HfO_x/TiN, PEALD HfO_x/TiN, TALD HfO_x/TiO_2 and PEALD HfO_x/TiO_2 heterostructures is classified under type I: straddling gap. A type I heterojunction is essential for the stacked material to act as a transistor gate dielectric, where the gate leakage is predicted to be negligible.[37]

Table 3: XPS analysis data for calculation of ΔE_V and ΔE_C of HfO_x/TiN and HfO_x/TiO_2, as well as measured E_g values of HfO_x and TiO_2. Error bar of XPS core level spectra lies within ±0.05 eV.

Sample ID	ΔE_V [eV]	E_g [eV]	ΔE_C [eV]
TALD HfO_x/ ALD-TiN	2.91	5.13 (HfO_x)	2.22
PEALD HfO_x/ ALD-TiN	3.28	5.02 (HfO_x)	1.74
TALD HfO_x/ TiO_2	0.44	5.13 (HfO_x)	1.70
		2.99 (TiO_2)	
PEALD HfO_x/ TiO_2	0.40	5.02 (HfO_x)	1.63
		2.99 (TiO_2)	

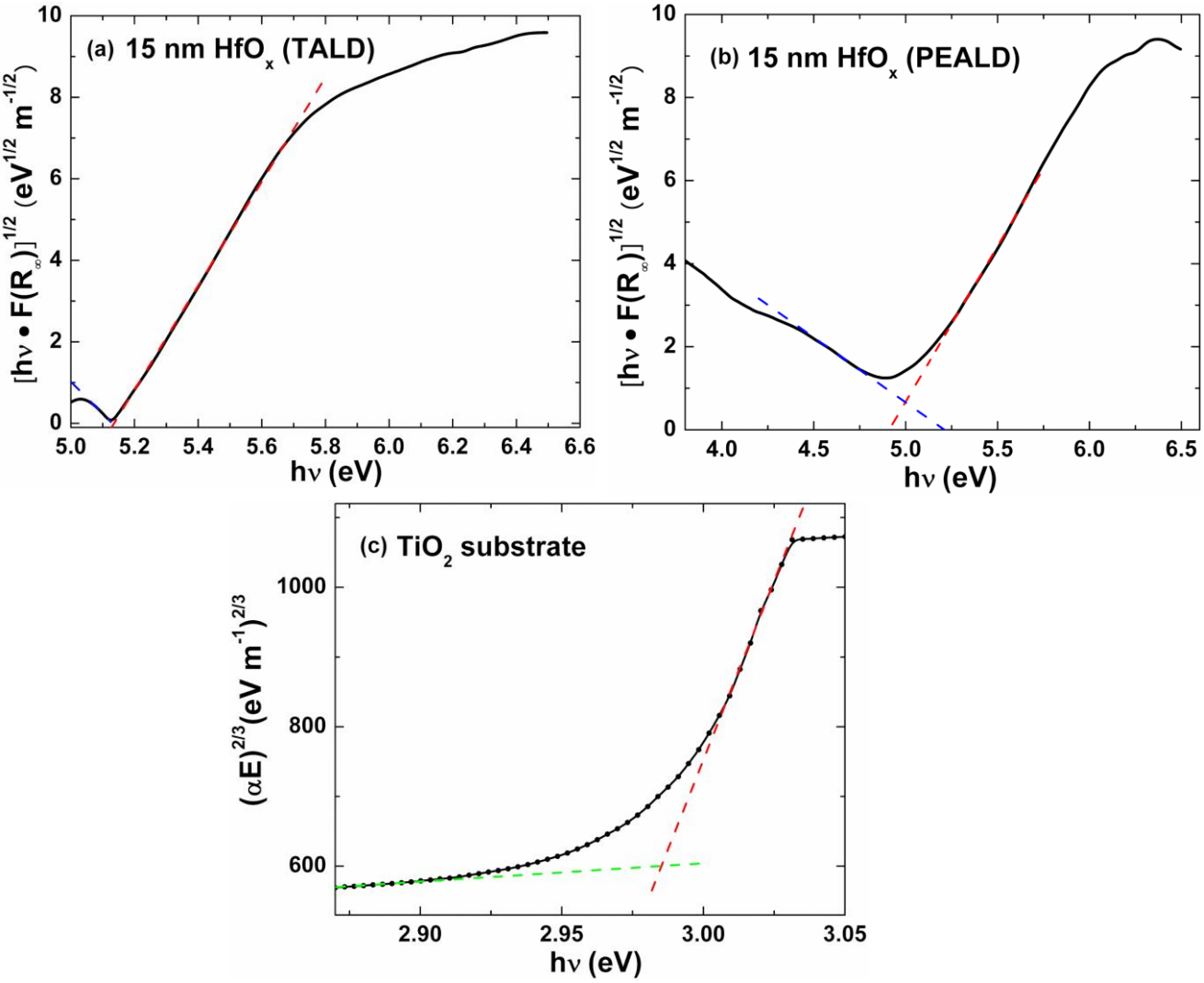
(a) 15 nm HfO$_x$ (TALD)
$[h\nu \bullet F(R_\infty)]^{1/2}$ (eV$^{1/2}$ m$^{-1/2}$)
hν (eV)
(b) 15 nm HfO$_x$ (PEALD)
$[h\nu \bullet F(R_\infty)]^{1/2}$ (eV$^{1/2}$ m$^{-1/2}$)
hν (eV)
(c) TiO$_2$ substrate
$(\alpha E)^{2/3}$(eV m^{-1})$^{2/3}$
hν (eV)

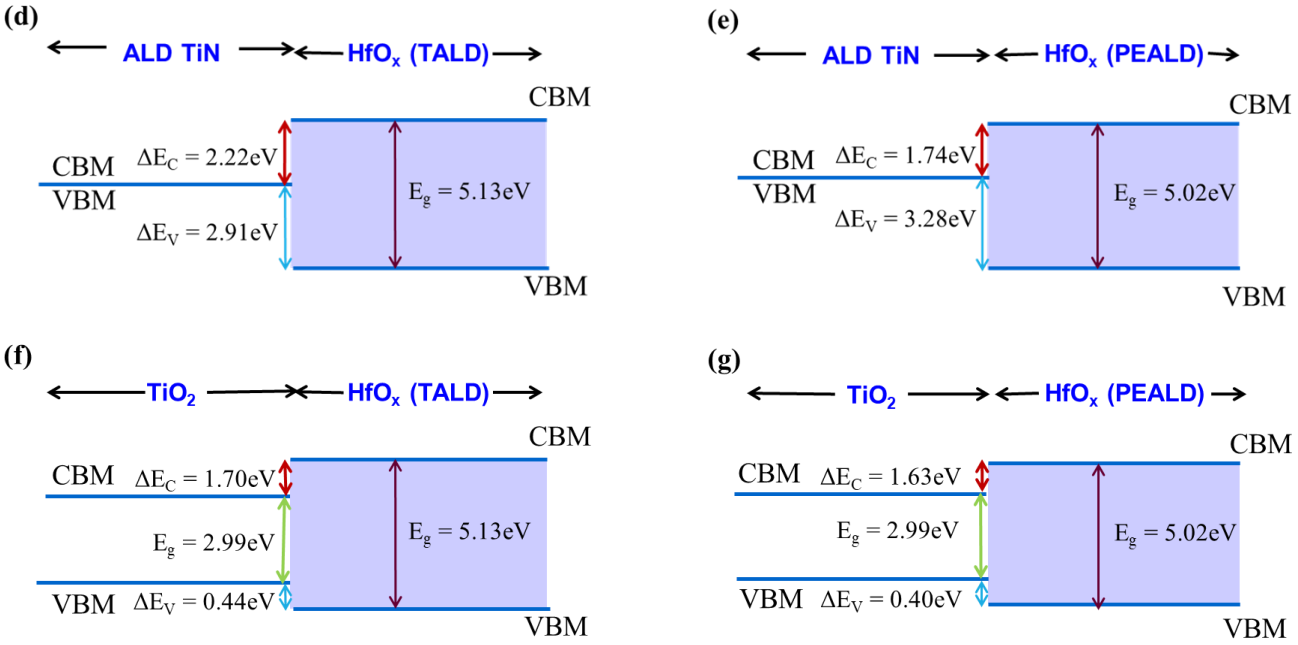
(d)
ALD TiN
HfO$_x$ (TALD)
CBM
CBM
VBM
ΔE$_C$ = 2.22eV
ΔE$_V$ = 2.91eV
E$_g$ = 5.13eV
VBM
(e)
ALD TiN
HfO$_x$ (PEALD)
CBM
CBM
VBM
ΔE$_C$ = 1.74eV
ΔE$_V$ = 3.28eV
E$_g$ = 5.02eV
VBM

(f)
TiO$_2$
HfO$_x$ (TALD)
CBM
CBM
ΔE$_C$ = 1.70eV
E$_g$ = 2.99eV
VBM
ΔE$_V$ = 0.44eV
E$_g$ = 5.13eV
VBM
(g)
TiO$_2$
HfO$_x$ (PEALD)
CBM
CBM
ΔE$_C$ = 1.63eV
E$_g$ = 2.99eV
VBM
ΔE$_V$ = 0.40eV
E$_g$ = 5.02eV
VBM

Figure 5. The optical E_g values for the 15 nm thick HfO_x deposited via (a) TALD and (b) PEALD, as well as the E_g value for (c) 0.1 cm thick TiO_2 annealed single crystalline rutile substrate, are extracted by fitting the absorption coefficients to the Tauc law. The corresponding linear fits are also shown. The schematic diagrams of the band offset at the HfO_x/TiN heterojunction interface for (d) TALD HfO_x and (e) PEALD HfO_x are depicted. Similarly, the schematic diagrams of the band offset at the HfO_x/TiO_2 heterojunction interface for (f) TALD HfO_x and (g) PEALD HfO_x are shown. The band alignment of the TALD HfO_x/TiN, PEALD HfO_x/TiN and TALD HfO_x/TiO_2 and PEALD HfO_x/TiO_2 heterostructures is classified under type I: straddling gap.

2.5 Electrical measurements of HfO_x/TiN RRAM stacks

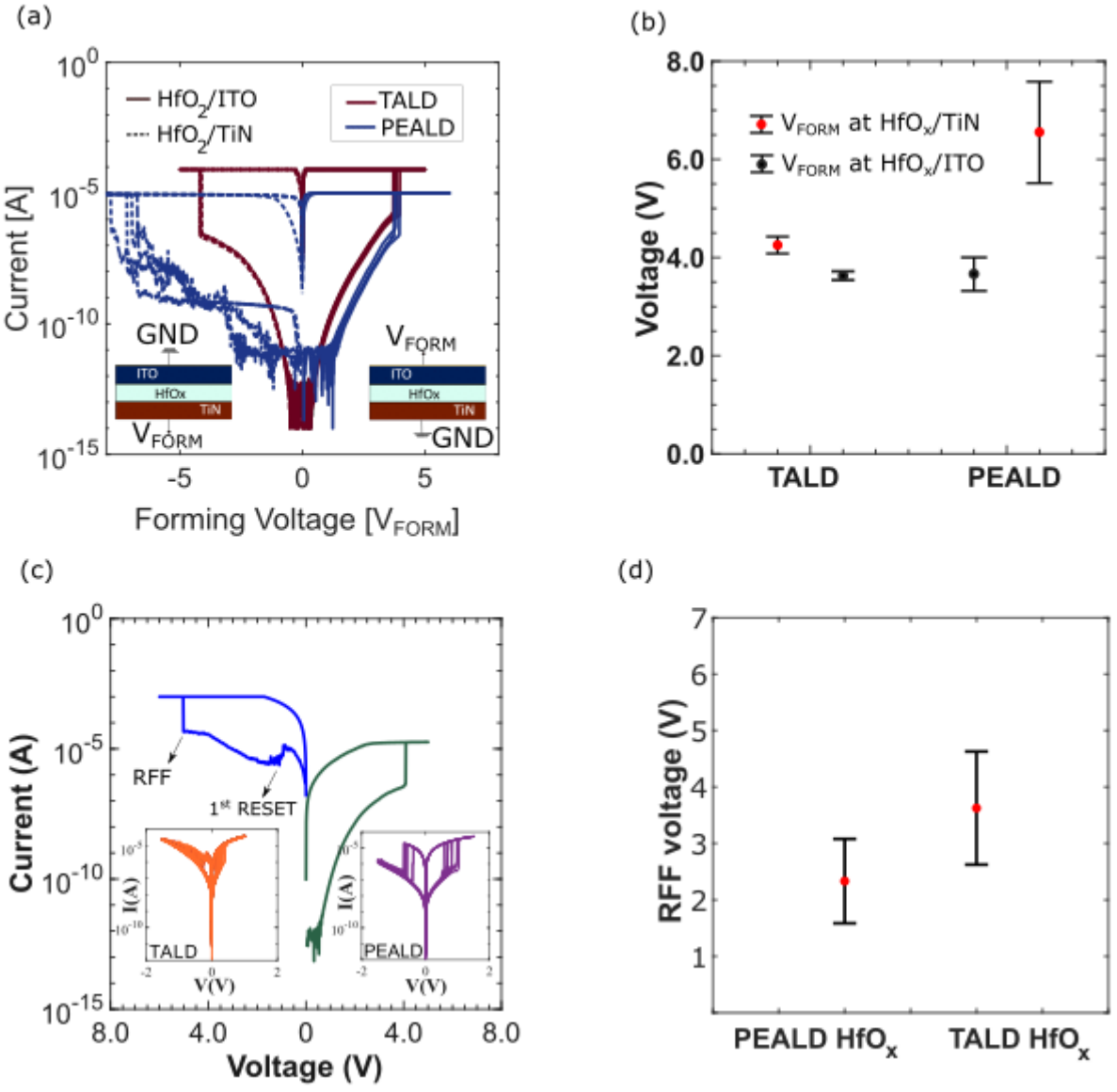

Figure 6. (a) I-V characteristics during FORMING for the TALD HfO_x RRAM using TiN and ITO as the electrical TME. (b) Forming voltage distribution for 5 devices at both interfaces for the TALD HfO_x RRAM. (c) I-V characteristics for the TALD HfO_x RRAM showing the 1st RESET and the onset of reverse filament formation. The inset figures show the DC switching I-V characteristics for the TALD as well as the PEALD

HfO_x. (d) RFF voltage distribution for 5 devices comparing the voltage at which RFF occurs for PEALD and TALD HfO_x samples.

To quantify electrically the effect of the HfO_x layer, ITO/HfO_x/TiN RRAM elements were fabricated and characterized. Figure 6a shows the I-V characteristics of the 2.5 nm TALD and PEALD HfO_x during the initial filament formation. The compliance current (CC) during the FORMING was kept below 80 µA to maintain compatibility with highly scaled vertical MOSFET selectors.[2, 4, 38] . Endurance measurement for up to 10^6 programming cycles for the TALD as well as the PEALD HfO_x sample was demonstrated previously and more stable switching was observed in the TALD HfO_x sample [41]. The relative switching instability in the PEALD HfO_x likely stems from the comperative findings in this study. To confirm the presence of the interfacial TiO_x layer in the PEALD HfO_x sample, the filament was first formed using the ITO as the electrical TME and then followed by using the TiN BME. As observed in Figure 6b, the forming voltage (V_{FORM}) for the TALD HfO_x at the ITO interface are found to be lower at 3.62 ± 0.09 V, as compared to the TiN interface to be 4.25 ± 0.17 V. On the other hand, V_{FORM} for the PEALD HfO_x at the ITO interface and TiN interface are found to be 3.7 V and 6.5 V, respectively. When comparing the PEALD HfO_x to the TALD HfO_x sample, it is observed that V_{FORM} at the ITO interface is similar for both samples whereas V_{FORM} at the TiN interface for the PEALD HfO_x sample is higher by ~ 2.0 V. The increase in V_{FORM} only at the TiN interface clearly indicates the presence of a thicker interfacial oxide (TiO_2) created by plasma oxidation of the TiN surface during PEALD of HfO_2.

Another method of electrically confirming the presence of the interfacial layer is by measuring the reverse filament forming (RFF) failure mechanism, which is caused by the supply of oxygen vacancies from the BME during the RESET operation.[5, 39, 40] Figure 6c shows the occurrence of RFF after the 1st RESET operation, while the inset figures show the conventional RRAM switching I-V characteristics. Figure 6d shows the cumulative distribution of the reverse filament forming voltage (V_{RFF}) for both the TALD and the PEALD HfO_x samples. With respect to RRAM operation, it is favorable to have the high-k/BME interface to be less reactive or inert as compared to the high-k/TME interface. This is desirable as it prevents RFF, which is initiated by a supply of oxygen vacancies from the high-k/BME interface. From Figures 5d and 5g, it can be noted that when the ΔE_C for the PEALD HfO_x sample is lowered by ~0.6 eV as compared to the TALD HfO_x sample, the margin for RFF for the PEALD HfO_x sample is reduced as seen in Figure 6d. This is presumably because the interface oxide layer (TiO_2) of the PEALD HfO_x sample acts as a reservoir in supplying excess

oxygen vacancies to the switching filament, thus resulting in RFF at a lower bias during the RESET operation, which is one of the primary causes for device failure impacting endurance cycles. Likely, the larger ΔE_C offset of the TALD HfO_x sample decreases the tunneling probability of the electrons, thereby lowering the rate of electron capture or emission by oxygen vacancies[41] and hence delays the onset of the RFF. This resulted in its V_{RFF} to be higher by > 1.0 V as compared to the PEALD HfO_x sample. Thus, the use of TALD HfO_2 would increase the margin for the onset of RFF, as well as improve endurance as demonstrated earlier.[42]

3. Conclusions

Two types of OxRRAM stacks were fabricated, both consisting of a PEALD TiN BME, a HfO_x switching oxide layer, and an ITO top metal electrode, and where the two types only differ by the fabrication procedures of the HfO_x switching oxide layer, using either TALD or PEALD. In the material investigation, XPS indicates a thicker interfacial TiO_2 layer in the PEALD HfO_x/TiN stack, as compared to the TALD HfO_x/TiN stack. As a result, the interface of the 2.5 nm PEALD HfO_x sample will resemble more of PEALD HfO_x/TiO_2 interface (ΔE_C = 1.63 eV and ΔE_V = 0.40 eV) whereas the interface of the 2.5 nm TALD HfO_x sample might be closer to TALD HfO_x/TiN interface (ΔE_C = 2.22 eV and ΔE_V = 2.91 eV). All the band alignment of the TALD HfO_x/TiN, PEALD HfO_x/TiN, TALD HfO_x/TiO_2 and PEALD HfO_x/TiO_2 heterostructures are classified under type I: straddling gap. Both the Hf 4*f* XPS spectra and VB studies reveal that the PEALD HfO_x is more oxygen deficient than the TALD HfO_x. In the electrical studies, the presence of the thicker TiO_2 interfacial layer in the PEALD HfO_x stack is further verified by the increase in the forming voltage and the early onset of RFF in the I-V measurements. This early onset of RFF is likely associated with a smaller ΔE_C, as compared to the TALD HfO_x/TiN stack. The application of TALD HfO_2 helps to raise the margin for the onset of RFF and improves endurance. Our results enhance the understanding of the high-k/BME interface which is vital when designing memory element material stacks for high performance.

4. Methods

4.1. Sample Preparation

Si substrates with thermally grown SiO_2 layers were used for the RRAM samples fabrication for device isolation and surface uniformity. ALD was used for deposition of the TiN BME at 250 °C. A tetrakisdimethylamido- titanium (TDMA-Ti) precursor and a 300 W N_2-plasma with 5 min /cycle were used. The BME was defined by photolithography and a SF_6/N_2 reactive ion etching process. A 2.5 nm thick HfO_2 which is used as the RRAM switching oxide was first deposited using PEALD (remote plasma) with a 300 W O_2 plasma at 200 °C. The process was then repeated under the same conditions using TALD with water vapour (H_2O) as the oxidant. The RRAM active area was defined by opening 3 µm-wide vias in the spacer layer defined by photolithography. ITO TME was deposited using sputtering with a 50 W RF power and 9 sccm Ar flow. The TME was then defined by photolithography followed by a Cl/Ar reactive ion etch. For improved probing during electrical characterization, W/Au contact pads were sputtered and patterned.

4.2 Characterization

XPS and valence band spectra were performed at a take-off angle of 50^o using a Thermo Fisher Scientific Theta Probe system which is equipped with a micro-focused, monochromatic Al Kα (1486.6 eV) X-ray source and a hemispherical electron energy analyzer. To compensate for issues with sample charging, a low-energy electron flood gun was used. Charge correction was performed using the position of C 1*s* spectra at 285.35 eV, which was the BE recorded at the Surface, Interface, and Nanostructure Science (SINS) beamline in Singapore Synchrotron Light Source (SSLS) after Au 4*f* BE calibration using gold foil. Analysis chamber base pressure was 5 x 10^{-10} mbar under ultra-high vacuum (UHV) condition. Shirley-type background subtraction was performed on Hf 4*f*, N 1*s* and Ti 2*p* spectra and they were subsequently fitted by mixed Gaussian–Lorentzian (G–L) functions.

In addition, diffuse reflectance measurements were carried out to measure the band gap of the 15 nm thick HfO_x samples using a Hitachi UH-4150 UV-Visible spectrometer, which is equipped with a 60 mm standard integrating sphere. Measurements were made with a slit width of 5 nm. On top of this, UV-Visible absorbance measurement for the 0.1 cm thick TiO_2 substrate was made using a Shimadzu UV-3101PC UV-Visible spectrometer. The TiO_2 substrate was loaded onto the sample holder and the absorbance was measured with an empty holder (air) as the reference. Slit width of 1 nm was used for the measurement.

The electrical measurements were performed on an Agilent B1500 parameter analyzer for DC characterization. Cross-sectional images of the active RRAM area were obtained using FEI Nova NanoLab 600 which is a combined focused ion beam and scanning electron microscope.

Acknowledgements

This work is financed through the Swedish Research Council grant no. 2016-06186 Electronics beyond kT/q (L.-E.W.).

Conflict of Interest

The authors declare no conflict of interest.

REFERENCES

1. Sebastian, A.; Le Gallo, M.; Khaddam-Aljameh, R.; Eleftheriou, E., *Nature nanotechnology* **2020,** *15* (7), 529-544.
2. Ram, M. S.; Persson, K.-M.; Irish, A.; Jönsson, A.; Timm, R.; Wernersson, L.-E., *Nature Electronics* **2021,** *4* (12), 914-920.
3. Ielmini, D.; Wong, H.-S. P., *Nature Electronics* **2018,** *1* (6), 333-343.
4. Persson, K. M.; Ram, M. S.; Kilpi, O. P.; Borg, M.; Wernersson, L. E., *Advanced Electronic Materials* **2020,** *6* (6), 2000154.
5. Yong, Z.; Persson, K.-M.; Ram, M. S.; D'Acunto, G.; Liu, Y.; Benter, S.; Pan, J.; Li, Z.; Borg, M.; Mikkelsen, A.; Timm, R.; Wernersson, L.-E., *Applied Surface Science* **2021,** *551*, 149386.
6. Kim, S. J.; Jung, Y. C.; Mohan, J.; Kim, H. J.; Rho, S. M.; Kim, M. S.; Yoo, J. G.; Park, H. R.; Hernandez-Arriaga, H.; Kim, J.-H., *Applied Physics Letters* **2021,** *119* (24), 242901.
7. Athle, R.; Persson, A. E.; Irish, A.; Menon, H.; Timm, R.; Borg, M., *ACS applied materials & interfaces* **2021,** *13* (9), 11089-11095.
8. Chen, P.-H.; Chang, K.-C.; Chang, T.-C.; Tsai, T.-M.; Pan, C.-H.; Lin, C.-Y.; Jin, F.-Y.; Chen, M.-C.; Huang, H.-C.; Wang, M.-H., *IEEE Electron Device Letters* **2016,** *37* (5), 584-587.
9. Persson, K.-M.; Ram, M. S.; Wernersson, L.-E., *IEEE Journal of the Electron Devices Society* **2021,** *9*, 564-569.
10. Kim, K.-M.; Jang, J. S.; Yoon, S.-G.; Yun, J.-Y.; Chung, N.-K., *Materials* **2020,** *13* (9), 2008.
11. Ahadi, K.; Cadien, K., *RSC advances* **2016,** *6* (20), 16301-16307.
12. Price, K. M.; Najmaei, S.; Ekuma, C. E.; Burke, R. A.; Dubey, M.; Franklin, A. D., *ACS Applied Nano Materials* **2019,** *2* (7), 4085-4094.
13. Yong, Z.; Linghu, J.; Xi, S.; Tan, H. R.; Shen, L.; Yang, P.; Hui, H. K.; Cao, J. Q.; Leek, M. L.; Yin, X., *Applied Surface Science* **2018,** *428*, 710-717.
14. Greczynski, G.; Hultman, L., *Applied Surface Science* **2016,** *387*, 294-300.
15. Greczynski, G.; Hultman, L., *Applied Physics Letters* **2016,** *109* (21), 211602.
16. Arranz, A.; Palacio, C., *Surface science* **2006,** *600* (12), 2510-2517.
17. Patscheider, J.; Hellgren, N.; Haasch, R. T.; Petrov, I.; Greene, J., *Physical Review B* **2011,** *83* (12), 125124.
18. Prieto, P.; Kirby, R., *Journal of Vacuum Science & Technology A: Vacuum, Surfaces, and Films* **1995,** *13* (6), 2819-2826.
19. Muneshwar, T.; Cadien, K., *Applied Surface Science* **2015,** *328*, 344-348.

20. Afshar, A.; Cadien, K. C., *Applied Physics Letters* **2013,** *103* (25), 251906.
21. Timm, R.; Head, A. R.; Yngman, S.; Knutsson, J. V.; Hjort, M.; McKibbin, S. R.; Troian, A.; Persson, O.; Urpelainen, S.; Knudsen, J., *Nature communications* **2018,** *9* (1), 1-9.
22. Perevalov, T.; Aliev, V. S.; Gritsenko, V.; Saraev, A.; Kaichev, V., *Microelectronic engineering* **2013,** *109*, 21-23.
23. Perevalov, T.; Aliev, V. S.; Gritsenko, V.; Saraev, A.; Kaichev, V.; Ivanova, E.; Zamoryanskaya, M., *Applied Physics Letters* **2014,** *104* (7), 071904.
24. Kraut, E.; Grant, R.; Waldrop, J.; Kowalczyk, S., *Physical Review Letters* **1980,** *44* (24), 1620.
25. Tauc, J.; Grigorovici, R.; Vancu, A., *physica status solidi (b)* **1966,** *15* (2), 627-637.
26. Davis, E.; Mott, N., *Philosophical magazine* **1970,** *22* (179), 0903-0922.
27. Kubelka, P.; Munk, F., *Z. Tech. Phys* **1931,** *12* (593), 193.
28. Eliziario, S.; Cavalcante, L.; Sczancoski, J.; Pizani, P.; Varela, J. A.; Espinosa, J.; Longo, E., *Nanoscale research letters* **2009,** *4* (11), 1371-1379.
29. Padma Kumar, H.; Vidya, S.; Saravana Kumar, S.; Vijayakumar, C.; Solomon, S.; Thomas, J., *Journal of Asian Ceramic Societies* **2015,** *3* (1), 64-69.
30. Makuła, P.; Pacia, M.; Macyk, W., How to correctly determine the band gap energy of modified semiconductor photocatalysts based on UV–Vis spectra. ACS Publications: **2018**.
31. Jayaraman, V.; Sagadevan, S.; Sudhakar, R., *Journal of Electronic Materials* **2017,** *46* (7), 4392-4397.
32. Cheynet, M. C.; Pokrant, S.; Tichelaar, F. D.; Rouvière, J.-L., *Journal of Applied Physics* **2007,** *101* (5), 054101.
33. Martínez, F.; Toledano-Luque, M.; Gandía, J.; Cárabe, J.; Bohne, W.; Röhrich, J.; Strub, E.; Mártil, I., *Journal of Physics D: Applied Physics* **2007,** *40* (17), 5256.
34. Graciani, J.; Hamad, S.; Sanz, J. F., *Physical Review B* **2009,** *80* (18), 184112.
35. Amtout, A.; Leonelli, R., *Physical Review B* **1995,** *51* (11), 6842.
36. Yamada, Y.; Kanemitsu, Y., *Physical Review B* **2010,** *82* (11), 113103.
37. Giampietri, A.; Drera, G.; Sangaletti, L., *Advanced Materials Interfaces* **2017,** *4* (11), 1700144.
38. Ram, M. S.; Persson, K.-M.; Borg, M.; Wernersson, L.-E., *IEEE Electron Device Letters* **2020,** *41* (9), 1432-1435.
39. Park, J.; Woo, J.; Prakash, A.; Lee, S.; Lim, S.; Hwang, H., *AIP Advances* **2016,** *6* (5), 055114.
40. Persson, K.-M.; Ram, M. S.; Borg, M.; Wernersson, L.-E. In *Investigation of reverse filament formation in ITO/HfO2-based RRAM*, 2019 Device Research Conference (DRC), IEEE: **2019**; pp 91-92.
41. Zeumault, A.; Alam, S.; Wood, Z.; Weiss, R. J.; Aziz, A.; Rose, G. S., *Frontiers in Nanotechnology* **2021**, 71.
42. Ram, M. S.; Persson, K.-M.; Wernersson, L.-E. In *Controlling Filament Stability in Scaled Oxides (3 nm) for High Endurance (> 10 6) Low Voltage ITO/HfO 2 RRAMs for Future 3D Integration*, 2021 Device Research Conference (DRC), IEEE: **2021**; pp 1-2.